



Flow regimes for liquid water transport in a tapered flow channel of proton exchange membrane fuel cells (PEMFCs)

Élton Fontana^a, Erasmo Mancusi^{a,b}, Antônio Augusto Ulson de Souza^a,
Selene M.A. Guelli Ulson de Souza^{a,*}

^a Universidade Federal de Santa Catarina, Departamento de Engenharia Química e Engenharia de Alimentos, 88040-970 Florianópolis, SC, Brazil

^b Facoltà di Ingegneria, Università del Sannio, Piazza Roma, 82100 Benevento, Italy

H I G H L I G H T S

- A 2D dynamic model is used to study the liquid water transport in a tapered channel.
- Typical operational conditions are assigned.
- The numerical mesh takes into account a channel with several liquid water inlets.
- The volume of fluid (VOF) method is used.
- Different flow regimes appear simultaneously in different channel regions.

A R T I C L E I N F O

Article history:

Received 17 September 2012

Received in revised form

27 January 2013

Accepted 30 January 2013

Available online 6 February 2013

Keywords:

CFD analysis

Multiphase flow

Volume of fluid

Tapered channel

Proton exchange membrane fuel cell

Water management

A B S T R A C T

The chemical species distribution inside a fuel cell is crucial to determining the cell performance. The use of tapered flow channels is recommended to improve the reactant distribution since it increases the pressure at the end of the channel, where the reactant concentration is reduced. In this study, a two-dimensional dynamic and isothermal model was used to numerically investigate the liquid water transport inside a tapered flow channel. Typical operational conditions were considered and the numerical mesh was constructed to represent the real fuel cell configuration, with several liquid water inlets characterizing the gas diffusion layer (GDL) structure. It was found that the liquid water distribution and transport inside the channel are dependent on the air velocity; different behaviors have been found along the channel. Near the channel outlet, the formation of a liquid film on the GDL surface is observed; in the central part and near the channel inlet the main form of liquid water transport is as slugs. Although responsible for an increase in the pressure drop, the slugs act as the main mechanism of water removal, removing attached droplets as they move toward the channel outlet and helping to reduce the water saturation inside the channel.

© 2013 Elsevier B.V. All rights reserved.

1. Introduction

Fuel cell energy generation systems have been receiving greater attention in recent years because of their high efficiency, low impact on the environment, lack of moving parts and superior reliability and durability. The conversion of chemical into electrical energy in fuel cell devices does not suffer from the Carnot

* Corresponding author. Chemical Engineering Department, Federal University of Santa Catarina, P.O. Box 476, Florianópolis, SC, CEP 88040-900, Brazil.

E-mail addresses: eliton.fontana@gmail.com (É. Fontana), mancusi@unisannio.it (E. Mancusi), augusto@enq.ufsc.br (A.A. Ulson de Souza), selene@enq.ufsc.br (S.M.A. Guelli Ulson de Souza).

limitations associated with classical heat engines. Moreover, proton exchange membrane fuel cells (PEMFCs), in which protons traverse a proton exchange membrane separating the anode from the cathode, are seen as the most attractive solution for automotive transportation and seem to be a good alternative source for distributed generation systems. PEMFCs can operate under several levels of energy demand, for example, for portable electronic devices, transport vehicles and residential power sources [1–4]. They have a high operational efficiency, low-temperature operation and relatively low demand for catalyst loads [5]. Moreover, when hydrogen is used as the fuel the only by-product generated is water. For these reasons PEMFCs are considered promising alternatives for the replacement of fossil fuel-based engines.

However, despite all of their advantages, the use of this technology in large scale is restricted due to several technical and operational issues. A crucial point to ensure the viability of the PEMFC operation is the water management inside the fuel cell. In fact, as discussed by Jiao and Li [6], a minimum level of hydration is required to facilitate efficient ionic conductivity in the proton exchange membrane. However, when the water content exceeds the saturation point the condensed water can induce flooding in the catalyst and gas diffusion layers, causing pore blockage and preventing the reactant from reaching the catalyst sites, decreasing significantly the fuel cell performance.

In recent years a large number of experimental research has focused on the water management inside PEMFCs, evaluating the influence of several parameters, for example, the hydrophobicity of the gas diffusion layer [7–9], the presence of a micro-porous layer [10,11] and the operational conditions [12]. By instantaneously measuring the flow rate, Owejan et al. [13] investigated the two-phase flow in parallel PEMFC channels and established a quantitative description of the channel flooding identifying different flow patterns. In particular, Lu et al. [14] found that, depending on the gas flow rate, three major liquid water flow structures are possible. To be more specific, for a gas flow rate ranging between 0.1 and 100 m s⁻¹ slug, film and mist flows are possible for low, intermediate and high gas flow rates, respectively. The presence of these flow regimes was also noted experimentally in an *in situ* visualization study of cathode-side flooding with the help of channel images by Hussiani and Wang [15].

At low gas flow rates the drag force is small and the droplet formation is controlled basically by the surface tension and therefore slugs or semi-slugs are randomly formed in the channels, leading to severe flow maldistribution. In fact, the slugs considerably increase the pressure drop along the channel, leading to significant pore blockage and thus decreasing the access of the reactants to the catalyst sites. The slugs or semi-slugs reside in the channels for periods ranging from several seconds to several hundreds of seconds, decreasing with increasing airflow rate [14,16]. At higher airflow rates, the two-phase flow is dominated by stratified/film flow in the case of hydrophilic channel walls. Under this condition the droplets in contact with the walls coalesce with other droplets prior to being dragged out of the channel. Since the channel is not significantly blocked by the water film, severe flow maldistribution is not found under the film flow regime. Under normal operating conditions, slug and film are the most common flow patterns, while mist flow is only observed for high air velocities. In mist flow, no variation in the channel flow rate and pressure drop can be detected, which indicates that tiny water droplets move at a velocity similar to that of the gas flow. The characteristics of droplet and film water motion in the flow channels of PEMFCs have an important influence on cell performance, but the transport mechanism is not clear.

In addition to experimental efforts, many attempts have been made to model and simulate the two-phase transport phenomena in PEM fuel cells. In this context, computer-based modeling and simulation are powerful tools to aid an understanding of PEMFCs and to deal with their complexity. The numerical approach helps to reduce the number of experimental tests required to study the cells systematically [17]. Simulation studies can determine the effects of various operating conditions, stack designs, cell temperature distributions, and thermal stresses, etc. In particular, computational fluid dynamics (CFD) is considered to be a very powerful tool in fuel cell design and operation optimization. In the early 2000s, liquid water transport was first incorporated in fuel cell modeling (e.g. Ref. [18]). Recently, more complex two-phase flow models have been applied to PEMFC modeling. The volume of fluid (VOF) method is suitable for tracing the trajectory of the liquid water

movement [6]. This method solves a single set of momentum equations, determining the volume fraction of each fluid along the domain [19]. The VOF method has been extensively used by Zhou et al. to analyze the flow channel flooding in the cathode of a PEMFC with different channel designs, for example, straight parallel [20,21], interdigitated [22] and serpentine [23,24] channels, and to investigate the droplet and film motion in the flow channel of a PEMFC [25]. However, due to the extremely small time-steps and intensive computing time related to VOF methods, their application has been restricted to investigating the liquid behavior in the electrode or flow channels (see Ref. [6] and references therein). Full geometry PEMFC models that incorporate the VOF approach have also been proposed [22,26], but only with very limited time instances considered due to the computational power limitation.

Most studies about the liquid water transport in flow channels have been focused on the behavior of pre-existing water droplets/films in the channels, without considering the emergence of water from the GDL (e.g. Refs. [27,28]) or, alternatively, only the presence of a single droplet or a single water inlet has been considered [e.g. Refs. [23], [29–31]]. However, under conditions of high current density the amount of liquid water generated can be significantly greater, leading to the formation of larger films and slugs, as observed in many experimental studies [e.g. Refs. [14–16]]. As the VOF method is very computationally expensive, the consideration of many droplets, as well as flow at low velocities, is limited. Quan and Lai [32] studied the effects of the hydrophobicity of channel surfaces, the channel geometry and the air inlet velocity on the behavior of water in a channel in which water originates from the whole surface of the GDL. The results indicated that the hydrophobicity of the reactant flow channel surface is critical for proper water management, since hydrophilic surfaces facilitate water transport along the channel surfaces or edges and also increase the pressure drop due to liquid water spreading. Ding et al. [33] showed that the use of a more hydrophobic GDL surface helps to expel water from the GDL surface, but may also increase the pressure drop. Ding et al. [34] also studied water motion in five different water injection structures. The results showed that a more hydrophobic GDL surface and/or more hydrophilic channel walls can enhance the transfer of the liquid droplets from the GDL surface to the channel walls. Zhu et al. [31] studied the dynamic behavior of liquid water entering a straight channel through a GDL pore via a 3D model, addressing the effects of the static contact angle, air flow velocity, water injection velocity and pore dimensions. The results obtained indicated that hydrophobic walls result in earlier detachment of water droplets, while hydrophilic walls lead to spreading of the water droplet on the GDL surface. Le et al. [24] studied liquid water behavior in a proton exchange membrane fuel cell cathode with serpentine channels and demonstrated that the key factors determining the shape and behavior of the droplets are the velocity of the air flow, contact angle, surface tension, and viscosity of the droplet. Recently, Cai et al. [35] studied the water motion in a simplified serpentine channel via a 3D model with five water inlet pores, addressing the effects of water emerging from one pore on the formation and subsequent behavior of water emerging from other pores as well as the effects of the hydrophobicity of the channel walls, the shape of the corner and the air inlet and water inlet velocities on the water behavior. Cai et al. [35] concluded that the volume fraction of water inside the channel decreases with increasing static contact angle whereas the facet fraction of the water on the bottom wall of the channel increases with increasing static contact angle. Moreover, the channel shape was found to play a significant role in the formation and motion of water droplets/films.

In this study, we numerically investigated the multiphase flow inside a tapered flow channel, considering the real channel

structure and normal operational conditions for PEMFCs. It should be noted that a numerical analysis of the water transport in a tapered PEMFC using a two-fluid model has been previously studied and validated by experimental results available in literature (Fontana et al. [36]), while the PEMFC model combined with the VOF method used in this work to simulate the mechanisms of fluid flow in a fuel cell channel were developed and experimentally validated by Le et al. [24]. The main difference between this work and previous studies is that several liquid water inlets are placed at the flow channel/gas diffusion layer (GDL) interface to represent the porous structure of the GDL, allowing the phenomena involved in the droplet coalescence and slug formation over time to be ascertained. The use of tapered channels has been recommended by many authors [36–40] to increase the pressure and the velocity of the flow near the outlet region, where the concentration polarization caused by the lack of reactants is usually greater. It was found that an inclination of 0.75° in a channel with a length of 5 cm can improve the maximum current density generated by almost 9.5%, with an increase in the maximum power density of 8% in comparison with the straight channel [36].

The model results are consistent with previously published experimental and computational observations regarding the water removal mechanism [14,43–47].

The article is structured as follows. In Section 2, the mathematical model for mass and momentum conservation and the numerical methodology used are described. In Section 3 the main results are discussed, showing the time evolution of the liquid water transport inside the channel and its impact on the pressure and velocity fields, and final remarks are given at the end of the paper.

2. Mathematical model and numerical methodology

To accurately describe the liquid distribution inside the flow channel a detailed mathematical model has to be used. In particular, such a model has to be able to capture the evolution of the interfaces between all of the phases. In this section, we firstly describe the mathematical model and then discuss how the water formation in the catalytic layer affects the boundary conditions between the GDL and the flow channel. Finally, the numerical methodology used in this study is discussed.

2.1. Mathematical model

The PEM fuel cell tapered channel model presented here is dynamic and isothermal. The geometry used to represent the tapered channel can be seen in Fig. 1, where the channel length/height proportion was rescaled to a ratio of 1/10 to facilitate the geometry visualization. To investigate the liquid water transport within the tapered flow channel, the volume of fluid (VOF) method was applied. This method considers the heterogenic nature of the multiphase flow, modeling two or more immiscible fluids with the use of a single set of momentum equations and determining the

volume fraction of each phase in the control volumes of the numerical mesh [19], considering most of the effects involved in the phase interface formation, such as the inertial forces, viscous forces, surface tension and gravitational effects, thus allowing the gas–liquid interface to be modeled.

The main model assumptions are listed below:

1. The flow is laminar, isothermal and incompressible;
2. The surface tension between the phases is constant, no Marangoni effect is considered;
3. The gas phase behaves as an ideal gas, which is consistent with the low pressures in the channel;
4. The mass transfer between the phases is neglected, thus the effects of water evaporation or condensation and gas absorption are not included.

To obtain the fluid flow and species transport, equations of conservation for mass, momentum and species (volume fraction) are solved. The continuity and the momentum conservation equations can be represented, respectively, as:

$$\frac{\partial \rho}{\partial t} + \nabla \cdot (\rho \mathbf{u}) = 0 \quad (1)$$

$$\frac{\partial (\rho \mathbf{u})}{\partial t} + \nabla \cdot (\rho \mathbf{u} \mathbf{u}) = -\nabla p + \nabla \cdot [\mu (\nabla \mathbf{u} + \nabla \mathbf{u}^T)] + \rho \mathbf{g} + \mathbf{F} \quad (2)$$

where \mathbf{u} is the velocity vector, p the pressure and \mathbf{g} the gravity vector, which in a two-dimensional case can be expressed as $\mathbf{g} = (0, g)$, where $g = 9.82 \text{ m s}^{-2}$. To capture the evolution of the interface between the phases, the volume fraction of each k th phase is computed. According to Zhu et al. [31], this volume fraction, C_k , can be expressed as:

$$C_k(x, y, t) = \begin{cases} 0 & \text{(outside the } k\text{th fluid)} \\ 1 & \text{(inside the } k\text{th fluid)} \\ 0 \sim 1 & \text{(at the } k\text{th fluid interface)} \end{cases} \quad (3)$$

The average density ρ and the average viscosity μ are determined considering the gas and liquid volume fractions in each control volume through linear interpolation. Considering the pure phase properties and denoting the gas phase by $k = 1$ and the liquid phase by $k = 2$, the average properties can be expressed as:

$$\rho = \rho_2 C_2 + \rho_1 C_1 \quad (4)$$

$$\mu = \mu_2 C_2 + \mu_1 C_1 \quad (5)$$

To compute the volume fraction of each phase in the control volumes, an additional continuity equation for the volume fraction is used. Based on this hypothesis (4), the equation for the volume fraction of the k th phase is given by Ref. [19]:

$$\frac{\partial (C_k \rho_k)}{\partial t} + \nabla \cdot (C_k \rho_k \mathbf{u}_k) = 0 \quad (6)$$

For the case of two-phase flow this equation has to be solved only for one phase, since the volume fraction of the other phase can be determined from the condition:

$$\sum C_k = 1 \quad (7)$$

In control volumes where $0 < C_k < 1$ the interface between the phases is found using the geometric reconstruction scheme. This method uses a piecewise-linear approach, assuming that the interface has a linear slope within the cells. The method refreshes the contact line based on the volume fraction of each phase in the

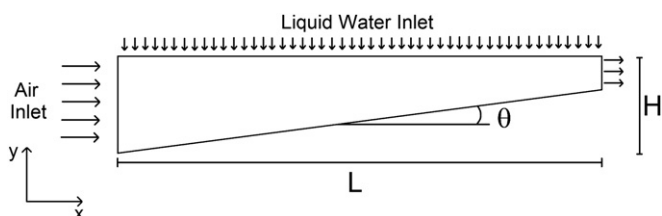


Fig. 1. Geometry used to represent the tapered channel (in scale of 1:10).

element adjacent to the wall, the velocity vector and the contact angle, so that the position of the interface in contact with the wall is recalculated at each iteration. Based on information on the volume fraction and its derivative, the position of the linear interface can be determined in each control volume, allowing the calculation of the fluid advection through the cell faces [19].

The pressure drop across the surface is a function of the surface tension between the phases, σ , with the relation given by the Young–Laplace equation:

$$p_2 - p_1 = \sigma \left(\frac{1}{R_1} + \frac{1}{R_2} \right) \quad (8)$$

where R_1 and R_2 are the orthogonal radii used to determine the surface curvature [19]. The surface tension is a fundamental parameter in this formulation as it determines the effect of the gas flow on the liquid transport. The force source term in the equation of momentum conservation (Eq. (2)) can be related to the surface tension with the use of the continuum surface force model. The expression obtained when only two phases are present in a cell is:

$$F = \frac{\sigma \kappa_k \nabla C_k}{0.5(\rho_1 + \rho_2)} \quad (9)$$

The surface curvature, κ_k , is defined as:

$$\kappa_k = \nabla \cdot \hat{n} \quad (10)$$

where the normalized vector \hat{n} is defined in all regions except in when the cells are adjacent to the walls, as:

$$\hat{n} = \frac{n}{|n|} \quad (11)$$

where n is the normal surface, defined in terms of the volume fraction gradient:

$$n = \nabla C_k \quad (12)$$

Due to the adhesion of the fluids to the walls, the normal surface for the cells near the walls is determined considering the static contact angle θ_w :

$$\hat{n} = \hat{n}_w \cos \theta_w + \hat{t}_w \sin \theta_w \quad (13)$$

where \hat{n}_w and \hat{t}_w are, respectively, the unit vectors normal and tangential to the wall. Based on Eqs. (11) and (13) it is possible to determine the local curvature of the surface over the whole domain. Considering that for a two-phase flow $\kappa_1 = -\kappa_2$ and $\nabla C_1 = -\nabla C_2$ [19], the set of Eqs (9)–(13) hold for both phases. The parameters used for the geometry, as well as the physical properties and the inlet conditions, are reported in Table 1.

The values reported in Table 1 are in agreement with data commonly presented in the literature. In particular, the contact angles can be found in Refs. [35,41], while the gas inlet velocity and channel geometry were reported in Refs. [36,42].

2.2. Boundary conditions

The upper porous wall represents the interface between the flow channel and the GDL and thus the liquid water enters the flow channel through this wall. To represent the porous structure of the GDL several inlet regions were distributed over the wall with a ratio between the water inlet area and the total upper part area of 0.1, resulting in a total of approximately one hundred liquid water inlets. This value is lower than the normal GDL porosity (0.3–0.7), however, it was selected due to the fact that a completely

Table 1
Parameters used in simulation.

Parameter	Value
<i>Geometric parameters</i>	
Channel height at air inlet, H	0.001 (m)
Channel length, L	0.05 (m)
Channel inclination, θ	0.75°
Pore diameter, d_p	50 (μm)
<i>Physical properties</i>	
Contact angle on the GDL (upper) wall, θ_w^{GDL}	135°
Contact angle on the channel (bottom) wall, θ_w^{FC}	90°
Surface tension, σ	0.066 (N m ⁻¹)
Operation temperature, T	333 (K)
Operation pressure, p	1 (atm)
Air inlet velocity, u_{air}	0.5 (m s ⁻¹)
Liquid water inlet velocity, u_l	0.0126 (m s ⁻¹)

homogeneous distribution of liquid water is not expected, but rather the formation of preferential channels for the liquid flow naturally occurs. The width of the water inlets used in the geometric design was $d_p = 50 \mu\text{m}$, which correspond to a normal pore diameter for the GDL. Now we need to address the inlet velocity of the liquid water. The liquid water inlet velocity adopted was based on an analysis of the total amount of liquid water generated in the cathode of a PEMFC under conditions of high current density. This velocity was determined using a nine-layer model to represent the entire fuel cell structure and a two-fluid model to determine the multiphase flow, as described in Fontana et al. [36]. It was found that for a cell operating at 60 °C the total amount of liquid water generated at the point of maximum power density corresponded to a liquid water inlet velocity of approximately $u_l = 1.26 \times 10^{-5} \text{ m s}^{-1}$. However, the VOF method requires very small time steps in order to keep the solution stable and the use of such small velocities as boundary conditions would require a great number of iterations that would prevent the capture of important phenomena in a viable time. To increase the liquid water velocity without interfering in the process of droplet formation, the relation between the forces involved were determined through the use of the following dimensionless numbers:

$$\text{Weber number : } We = \frac{\rho_2 u_l^2 d_p}{\sigma} \quad (14)$$

$$\text{Capillary number : } Ca = \frac{\mu_2 u_l}{\sigma} \quad (15)$$

$$\text{Bond number : } Bo = \frac{(\rho_2 - \rho_1) g d_p}{\sigma} \quad (16)$$

These numbers represent, respectively, the relation between the inertial, viscous and buoyancy forces in comparison with the surface tension force. The values obtained with the physical parameters and boundary conditions used are: $We = 1.18 \times 10^{-10}$, $Ca = 9.07 \times 10^{-8}$, $Bo = 3.65 \times 10^{-4}$ thus the surface tension forces are considerable higher than the other forces. Considering that the Bond number is not dependent on the liquid water inlet velocity, we can observe that this velocity can be increased by the order of 10^3 – 10^4 without altering the predominance of the surface tension force. Based on these considerations, the liquid water inlet velocity was increased by a factor of 10^3 to allow the numerical simulation in a reasonable time. This increase does not change the physics of the problem, indeed the surface tension is still the predominant effect, while the time range that we need to simulate numerically is reduced.

Finally, the air inlet velocity was set at 0.5 m s^{-1} , corresponding to the typical velocity adopted in fuel cell systems. It is well known that a higher velocity increases the liquid water removal, but the

parasitic losses generated usually inhibit the use of high velocities. No-slip conditions were used on all walls and the initial state was set to $\mathbf{u} = 0$ and $\rho = \rho_1$.

2.3. Numerical procedure

In the ANSYS Fluent software the differential equations are discretized using the finite volume method. To solve the set of algebraic and partial differential equations previously presented, a non-uniform two-dimensional structured mesh was built based on the proposed geometry. This kind of mesh is used due to the relatively simple geometric configuration of the channel, as a more complex mesh structure is not required. Moreover, structured meshes are usually less computationally expensive and require a smaller number of iterations to achieve the desired convergence. To determine the necessary refinement, the influence of the mesh size on the process of droplet formation was analyzed. It was determined that a mesh with 90×7000 elements (630,000 cells) is sufficiently refined to represent this process. This is a very high number of cells; however, in view of the small pore diameter a large number of cells are necessary to capture the formation of droplets around each liquid water inlet.

To solve the pressure–velocity coupling, the Pressure-Implicit with Splitting of Operators (PISO) scheme was used. This scheme allows increased values for all under-relaxation factors in comparison with the SIMPLE and SIMPLEC schemes, making the solution process quicker without losses of stability. The QUICK scheme was used as the interpolation function for the momentum equation. This scheme represents a weighted average of second-order upwind and central interpolation formulations and typically represents an accurate interpolation in structured meshes aligned with the flow direction [19]. For the transient discretization a first-order implicit formulation was used. To accelerate the solution convergence an algebraic multigrid method was applied, where a hierarchy of discretization was used to quickly reduce both oscillatory and smooth errors. In the multigrid formulation, the F-cycle was used with termination criteria of 10^{-3} for all variables. Appropriate under-relaxation factors were set for all variables in order to keep the solution stable. The solution was considered converged when the error associated with each variable was less than or equal to 10^{-4} in each time step. The values of the time steps were determined based on the physical conditions of the system through the use of the Courant number [19]. The value of this dimensionless parameter was fixed at $Co = 3$, which ensured a stable solution. These values correspond to time steps of the order of 10^{-6} – 10^{-8} s, depending on the flow conditions. The model results are in agreement with previously published experimental and computational observations [14,43–47].

3. Results and discussion

In this section an analysis of the droplet formation, coalescence and detachment is presented. In particular, the effect of the gas velocity on the liquid water behavior is discussed in depth. In the fuel cell, water can enter the gas flow channels from the gas diffusion layer (GDL) and the evolution of the droplets is a crucial point in terms of understanding the development of two-phase flow. Basically, the forces acting on a droplet attached to the GDL surface can be summarized as drag forces and surface adhesion forces. The drag is the sum of the shear stress and pressure force and it induces the liquid transport, while the surface adhesion force is the component of the surface tension which tends to keep the droplet held in place. If the drag force balances the adhesion force, the droplet will not be removed and the droplet is considered stable. Increasing the drag force until it is greater than the adhesion

force can cause instability, allowing the droplet to be detached from the GDL. Once detached, the droplet moves along the GDL surface, where it can combine with other droplets to form slugs. As the drag force is strongly dependent on the air velocity and droplet size, different behaviors are expected for different regions along the tapered channel since in this type of geometry the air velocity changes along the channel due to the reduction in the cross-sectional area. Therefore, to aid the discussion we divided the PEMFC channels into three regions. As will be discussed below, the flow characteristics and the time scale involved in the process of liquid transport are different along the flow channel.

All of the results presented in this section were obtained based on the parameter values reported in Table 1. In particular, the contact angle of the liquid at the interface with the lower wall was considered to be 90° and the GDL was 135° , thus corresponding to a hydrophobic surface. The latter value is an important parameter in determining the solid–fluid interaction. In the case of hydrophobic surfaces the adherence of liquid hinders the formation of films. Therefore, smaller contact angles facilitate the formation of films [e.g. Ref. [48]].

3.1. The effect of the gas velocity

The production of liquid during the electrochemical reaction leads to the appearance of liquid water along the entire fuel channel in the form of spherical droplets attached to the GDL wall. In fact, initially, the small droplets show approximately a spherical shape due to the predominance of surface tension forces with respect to shear forces. The recently formed droplets can detach and be transported by the gas stream or grow in size. When the droplets are small the detachment occurs separately, that is, without the droplets forming agglomerates of liquid and these small liquid droplets are dragged out of the gas stream. Since the fuel cell operates continuously the liquid water inlet is constant, which leads to a proportional increase in the droplet size over time. As the droplets increase they can coalesce and be dragged out from the channel as a slug or film. Although the behavior of small droplets is similar along the entire channel, differences can be observed as regards the coalescence and the formation of a slug or liquid film. In the tapered channel the gas velocity increases as the gas approaches the channel outlet. Thus, the effect of the gas velocity on the droplets is more evident close to the end of the channel and is delayed close to the beginning. We start our discussion by showing firstly the end section of the channel. This is the region where greater velocities are achieved and thus this is where droplet deformation and detachment are observed sooner. In Figs. 2–4 the liquid water behavior for different time values is reported. Unless otherwise specified, the reported time is dimensionless ($t^* = t u_l / H$). The physical time range that we explored was between 0.0 and 4.6 s.

In Fig. 2 the channel section close to the exit is represented. As discussed above, at the beginning (Fig. 2a) a predominant homogeneous growth is observed along the channel fraction represented. The droplets have a predominately spherical shape due to the predominance of surface tension forces. As a result of the increase in the size of the droplets the velocity of the gas increases due to a reduction in the free section. Greater velocities correspond to higher shear forces. This induces the deformation and detachment of droplets, as can be seen in Fig. 2b. This phenomenon quickly appears close to the end of the channel where the gas velocity reaches its highest values. In this section the droplets do not interact and are removed separately. Further from the channel outlet the lower gas velocity allows the droplets to reach a greater size without being dragged out by the gas flow. When the droplets reach a sufficiently large diameter the phenomenon of coalescence

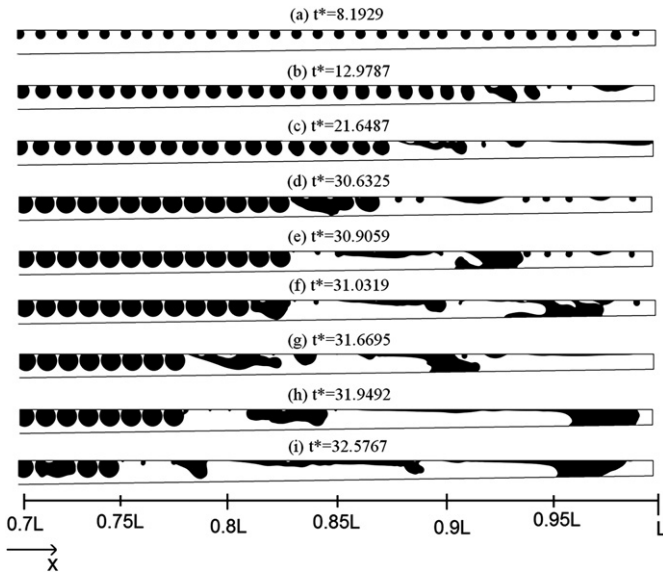


Fig. 2. Temporal evolution of droplet formation and transport in the final part of the flow channel.

can be observed. Further away from the channel outlet the coalescence is observed later. As can be observed in Fig. 2, firstly, the initial droplets coalesce into larger ones and then they are dragged out of the channel (the process of droplet coalescence will be discussed in greater detail in Section 3.2). The liquid water detachment from the GDL surface is not observed, but the transport occurs as a film adhered to the GDL surface. The adhesion to the wall makes the film more difficult to remove than the slugs, increasing the residence time of the liquid water. Moreover, this is an undesirable transport mechanism because it generates pore blockage. Even after the removal of most of the liquid water that forms these films, some regions remain blocked by small films adhered to the GDL surface. The film formation is dependent on the gas velocity, appearing only in a region near the end of the channel, where the velocities are higher.

The agglomeration of droplets induces the formation of the structures known as slugs, which means a significantly large amount of liquid water moves through the channel covering a great part of the channel height. These structures can be observed in Fig. 2d–i. Slugs initially appear due to the coalescence of the droplets closest to the channel outlet that have not yet been removed by the gas flow. Over time, the droplets nearest to these coalesce and also form slugs, originating a continuous process of water removal as small slugs. It is worth noting that these initial slugs are formed by a small number of droplets, thus presenting a relatively small size. However, even small slugs fill the entire channel height, blocking the air flow and increasing considerably the pressure drop, as will be discussed later. We can observe that the process of slug formation and transport along the channel is much faster than the process of liquid droplet formation and growth. As the slugs are transported along the channel they capture small droplets that begin to reappear on the GDL surface, hindering the formation of large droplets near the outlet and helping to reduce the amount of liquid water present in the channel. However, as the slugs flow over the GDL surface, the development of liquid water films on this surface can be observed, despite the hydrophobic nature of the GDL. As previously discussed, the film formation only occurs in high-velocity regions and thus it is confined to the final part of the channel.

In Fig. 3 several time steps for the middle part of the channel are presented. The gas flow velocity in this section is lower than in the

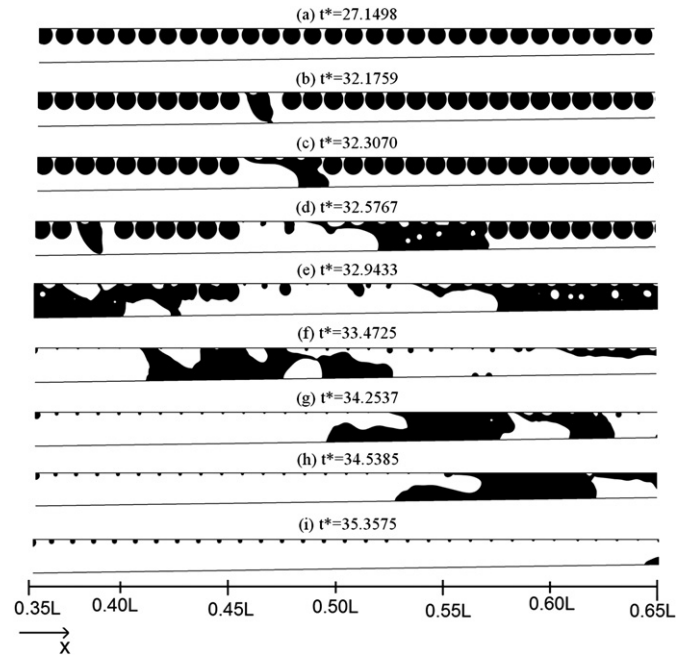


Fig. 3. Temporal evolution of droplet formation and transport in the central part of the flow channel.

final part and therefore the shear forces acting on the droplet surface are reduced, increasing the time required for the processes of droplet detachment and slug formation to begin. It is important to note that, in contrast to the final part of the channel, in this section we do not observe the presence of liquid film and the coalescence appears erratically along the channel. Prior to the time reported in Fig. 3a no notable event related to the liquid droplets occurs, but as time passes the first coalescence is observed in the middle of the represented section and not close to its end, as can be seen in Fig. 3b and c. The larger droplets formed in this coalescence process have a larger superficial area, causing an increase in the drag force. Due to this force the mass of liquid water moves toward the channel outlet, coalescing with many other large droplets along the way and forming a large slug, as observed in Fig. 3d–h. These slugs are considerably larger than those shown in Fig. 2. As the slugs move and capture other droplets the free space between them is incorporated into the slug structure in the form of small bubbles. These bubbles tend to move upward in the liquid water as a result of the buoyancy force. In the smaller slugs shown in Fig. 2 the presence of bubbles was not noted, which may be due to the fact that these slugs do not fill the entire channel height and so when the slug captures the droplets there is no free space in the slug structure. Note that the time step represented in Fig. 3d corresponds to the last time step in Fig. 2; however, the influence of the slug formation in the middle part does not affect significantly the liquid water behavior near the channel outlet before this time step.

In contrast, the influence of the initial part of the channel on the liquid water behavior in the middle part can be clearly seen in Fig. 3e–h, where a slug originating from the initial part of the channel can be observed. This slug flows in a region where some of the droplets formed in the initial time steps are no longer attached to the GDL surface and larger spaces of air appear in the slug structure. As it moves toward the outlet, a greater adhesion is observed on the bottom wall, which is consistent with the hydrophobic nature of the GDL surface. In contrast to the behavior observed for the final part of the channel, in the middle part the slug passage does not induce the formation of a liquid film on the upper

surface. Pure slug flows are common for low air velocities, which indicate that the decrease in the air velocity caused by the channel enlargement is sufficient to avoid the film formation. After the slug passage only small newly formed droplets can be seen, indicating that the flow configuration almost returns to its initial state.

The evolution of the droplets over time in the initial part of the channel section can be seen in Fig. 4. As in the central part, in the initial part the droplet coalescence does not occur initially at the extremities, but appears firstly in some intermediary region, as shown in Fig. 4a. As a result of the relatively low air velocity the large droplets formed in the coalescence process are not quickly dragged out, but remain attached to the GDL surface and keep growing due to the liquid water inlet, as can be seen in Fig. 4b–d. However, when the mass of liquid water reaches a sufficiently large size to be dragged out, the formation of a slug occurs, as observed in Fig. 4e. This size is dependent on several factors, such as the position of the droplet in the channel, the gas velocity on the surface, the presence of gas recirculation, and the structure of the flow inside the droplets, which makes it difficult to determine a single value for the droplet size at which detachment occurs.

The slugs formed after droplet detachment move toward the channel outlet capturing more droplets and increasing in size, as previous described. The last time steps in Fig. 4 show that after a relatively long time the larger droplets generated near the channel inlet remain attached to the GDL surface for a relatively long time, being removed only after reaching a relatively large size. This kind of behavior is expected in a straight channel, where the lower velocities allow the stability of larger droplets. Therefore, the inclination of the bottom wall of the channels hinders the accumulation of liquid water, favoring the formation of slugs that are quickly removed and so the fraction of liquid water inside a tapered channel is expected to be smaller. This represents an improvement in the water management in comparison with the straight channel.

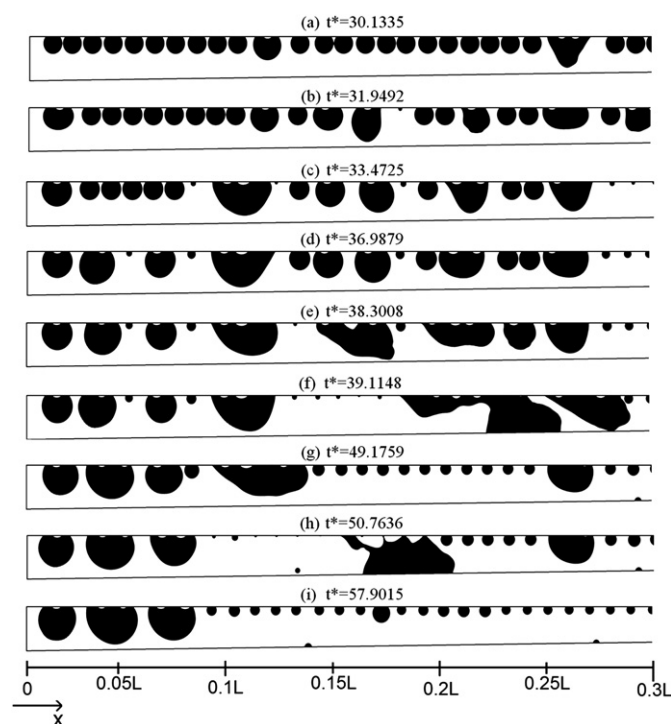


Fig. 4. Temporal evolution of droplet formation and transport in the initial part of the flow channel.

3.2. Droplet coalescence and slug formation

The droplet interaction which occurs on the GDL surface is crucial to determining how the liquid water will be dragged out of the channel. As observed in Figs. 2–4, the droplet coalescence is an important phenomenon that can be observed along the entire channel. In Fig. 5 the evolution over time of two droplets attached to the GDL surface is reported. For the sake of clarity the velocity vectors represented are normalized.

Initially, (Fig. 5a and b) the homogeneous growth of the droplets can be observed. It should be noted that the results given in Fig. 5 refer to the central part of the channel section, but the coalescence phenomenon occurs regardless of the channel position. The flow inside the droplets is represented by two anti-symmetric eddies, with the liquid flowing downstream in the central region and upstream in the lateral region. This behavior is expected when the flow structure inside the droplets is mainly determined by the liquid water inlet velocity and the surface tension forces; thus, the shear forces induced by the air flow are negligible. As the size of the droplets increases they can coalesce (Fig. 5c). Under these conditions we can see that the liquid flows toward the point of contact, forming a bridge between the droplets and originating a capillary wave that travels along the droplet surface. The height of this bridge rapidly increases due to the fluid inertia forces and eventually becomes larger in diameter than the initial droplets, as can be seen in Fig. 5d and e. Over time the coalesced droplet continues to increase in height (Fig. 5d and e). This is essentially due to the tendency of the liquid water to move from the boundary to the center of the new droplet. Under the effect of this fluid motion the coalesced droplet becomes deformed and increases up to a maximum height (Fig. 5f). On the other hand the inertial forces start to push back the liquid close to the surface again, causing a reduction in the droplet height, as can be observed in Fig. 5g. This results in an overdamped oscillatory response for the droplet height. A similar behavior has been described by Kapur and Gaskell [47]. After the oscillation stabilizes the droplet has a spherical shape as a result of the predominance of surface tension forces. The droplet keeps growing due to the incoming liquid water and in Fig. 5i we can observe that the shear caused by the air flow induces the formation of a well-defined single anti-clockwise eddy inside the droplet, in contrast to the anti-symmetric eddies observed for the small droplets.

One of the most notable influences of the droplet coalescence is the formation of slugs, which is the most significant mechanism of liquid water removal, especially for later time steps. These slugs are not formed from hydrodynamic instabilities, but result from the combined effects of the droplet agglomeration and the channel constraint. Fig. 6 shows the formation of a slug over time and its transport along the channel. At the beginning (Fig. 6a and b) we can observe the coalescence of some droplets to form a larger liquid agglomerate. It is important to note that because of the small distance between the liquid water inlets the coalescence occurs between droplets with a diameter smaller than the channel height. The liquid water is pushed down by the effect of gravity and touches the bottom wall, covering the whole channel height (Fig. 6c). After this point this mass of liquid water is dragged along the channel and captures other droplets, effectively forming the slug. Initially, the slug is not well defined and a flow pattern of liquid and air is formed, as can be seen in Fig. 6e, but as it moves along the channel these spaces disappear and a homogeneous liquid structure can be observed near the channel outlet (Fig. 6f–h). Note that when the slug moves through the central part of the channel (Fig. 6f and g) there is no film formed on the upper wall, with a greater elongation near the bottom wall due to a smaller static contact angle. However, in the final part of the channel (Fig. 6h), a film appears on the upper wall after the slug passage, as

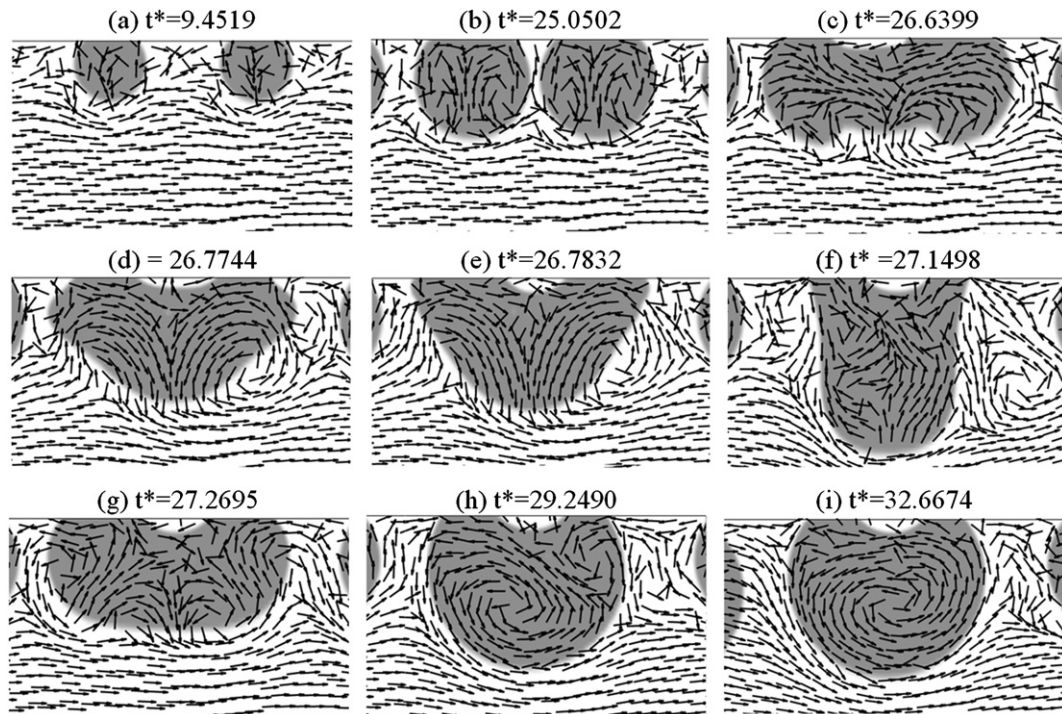


Fig. 5. Droplet coalescence.

can be noted in Fig. 2. This film, as discussed above, only appears close to the channel outlet.

3.3. Wall coverage and water saturation

The presence of liquid water in the flow channel causes pore blockage and therefore information on the dynamic behavior of the liquid water in contact with the GDL surface is essential in order to understand the importance of the multiphase model in evaluating the overall fuel cell performance. The evolution of the wall coverage (fraction of wall covered by liquid water) over time for the upper and bottom walls is shown in Fig. 7. For the upper wall we can observe a practically linear increase during the initial time interval

due to the homogeneous droplet growth, which causes a slow covering of the wall near the droplets. For $t^* \approx 30$ a rapid decrease can be seen, indicating the removal of a significant amount of liquid water and on observing the results presented in Figs. 2–4 we can note that this corresponds to the formation and transport of larger slugs. Although they are responsible for the channel blockage the slugs are the main mechanism of water removal in this case and thus they do not adversely affect the fuel cell performance.

After the wave of slug removal the upper wall coverage continues to increase linearly, with some oscillations due to slug removal and droplet detachment. This behavior can be clearly seen when we analyze the bottom wall coverage. During the initial period the bottom wall remains uncovered since along the entire

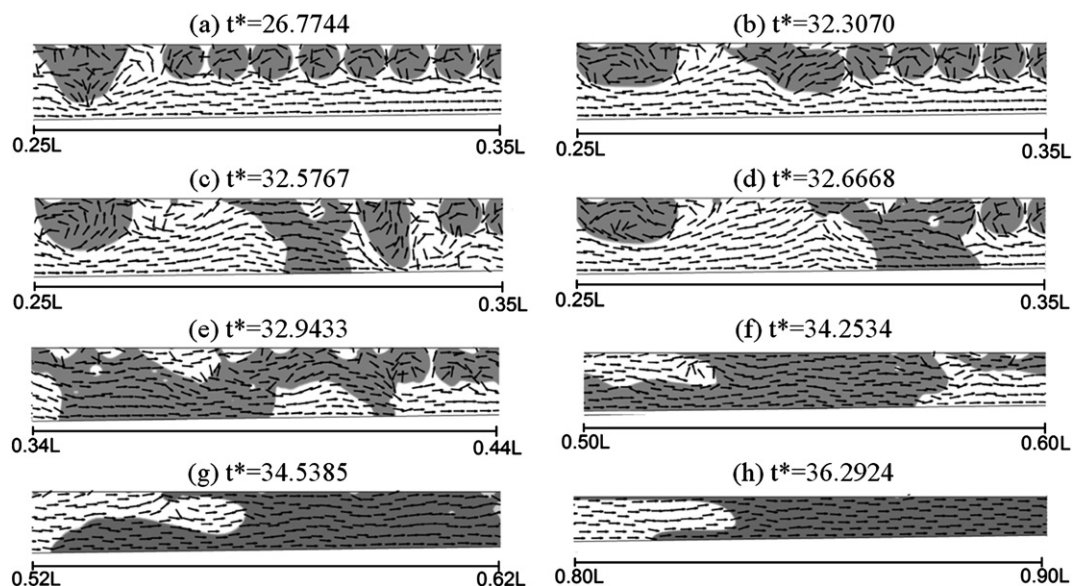


Fig. 6. Slug formation and transport.

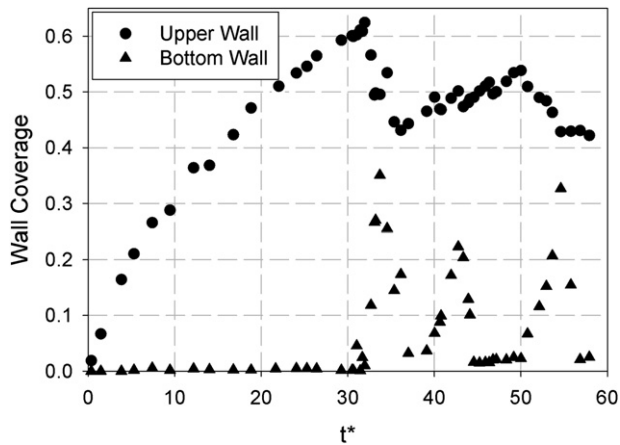


Fig. 7. Bottom and upper wall coverage.

channel the diameters of the growing droplets are smaller than the channel height. When the formation of large slugs begins ($t^* \approx 30$) the bottom wall coverage quickly increases, reaching a maximum value and then rapidly decreasing to practically zero again. In this case the increase corresponds to the slug formation and the decrease occurs when the slugs leave the channel. After some time, a second and third peak in the bottom wall coverage is observed, corresponding to further waves of slug removal.

In addition to the wall coverage, the total amount of liquid water present inside the channel is a significant factor in relation to the fuel cell performance, directly affecting two important points, the pore blockage and the pressure drop. The water saturation (volume fraction of liquid water) as a function of time is presented in Fig. 8. A behavior similar to that observed for the upper wall coverage can be seen in this case, with an initial linear increase as a result of the homogeneous droplet growth. When the first slugs begin to appear ($t^* \approx 30$) the increase stops and, in contrast to the upper wall coverage, the water saturation remains constant for some time and then rapidly decreases. On observing Fig. 2, we can see that for t^* values between 30 and 32 there is the formation of small slugs in the final part of the channel, which are quickly dragged out. During this stage the amount of liquid water dragged out is comparable with the amount of water that enters from the liquid water inlets and so the water saturation remains almost constant. While the large slugs are being dragged out the water saturation quickly decreases. It then increases after this point and decreases again when

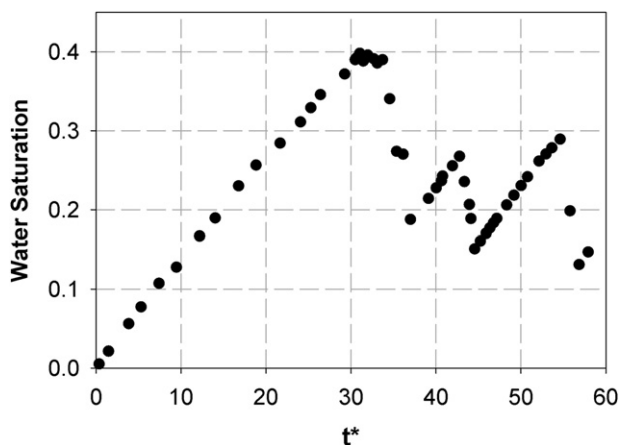


Fig. 8. Liquid water fraction in the channel as a function of time.

other slugs are removed. Thus, we can observe a repeating process involving an increase in the water saturation until the formation of slugs followed by a fast decrease due to the slug removal. As previously discussed, the bottom wall inclination induces the formation of slugs early and firstly near the channel outlet, thus reducing the average time in which the liquid water remains inside the channel in comparison with a straight channel. For a straight channel with the same operational conditions we can expect greater water saturation before the slug formation begins and thus the time interval between the cycles of water saturation increase/decrease will be longer.

3.4. Pressure drop and velocity distribution

The main problem associated with the slug formation is the increase in the pressure drop along the channel. The total pressure drop as a function of time is shown in Fig. 9. The influence of slugs on the pressure drop can be clearly seen in time intervals with a greater concentration of high pressure drop points. As will be discussed below, the pressure is greater in the liquid phase than in the gaseous phase and depending on which fluid is at the channel outlet the pressure can be determined in the liquid or gaseous phase, which causes the oscillation observed at the points with a higher pressure drop. Despite the small increase noted for $t^* < 30$, the pressure drop only changes significantly when the slugs begin form. In the time interval between $t^* = 30$ and $t^* = 35$ we can observe an increase, by a factor of 20, in the pressure drop, which cannot be neglected due to the associated costs related to the requirement for a compression system. Similar points of high pressure drop can be observed for the other stages of slug removal.

The pressure profile along the central line of the channel for some selected time steps, as well as the corresponding liquid water distribution in the channel, is presented in Fig. 10. The channel geometry was resized to facilitate the visualization of the entire channel, with an enlargement of 10 times in the y direction. The time step shown in Fig. 10a represents the first step when liquid water occupies the entire channel height at some point. As can be seen in the pressure profile, this causes a much higher pressure drop than that observed in the rest of the channel. The oscillatory behavior of this profile is caused by the passage of the central line in a region with droplets attached to the GDL wall and gaps between the droplets. The pressure in the liquid phase is higher than in the gaseous phase, causing the oscillation in the pressure profile.

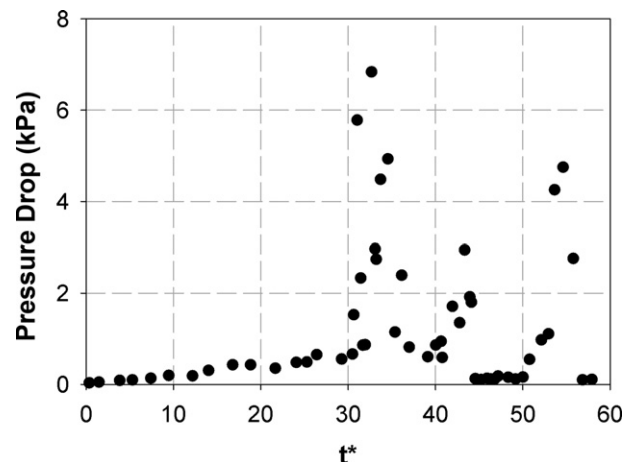


Fig. 9. Pressure drop over time.

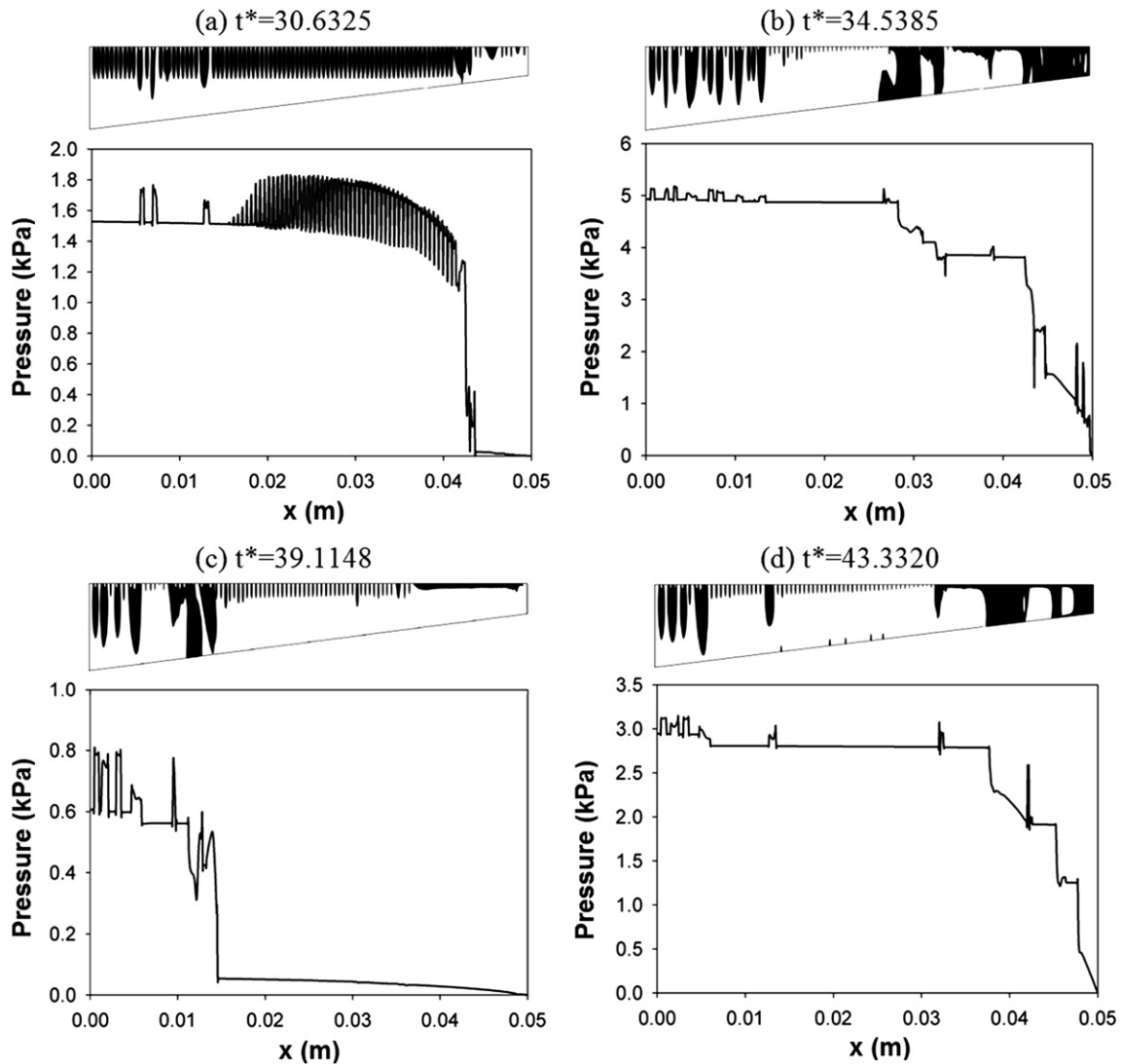


Fig. 10. Liquid water presence within the channel (upper part) and pressure profile along central line of the channel for selected time-steps.

The time step shown in Fig. 10b has a higher pressure drop, corresponding to the first wave of slug removal mentioned above. In this case two main slugs can be observed, originating two regions of significant pressure drop along the channel. In particular, the slug near the channel outlet causes a drop of more than 3.5 kPa, which is greater than any other drop found in this case. Fig. 10c shows a case where only a small slug in the initial part of the channel is observed, which causes a much smaller pressure drop in comparison with the other cases. This time step corresponds to an interval between two waves of slug removal. As this mass of liquid water moves through the channel the pressure drop increases until a point where it is about 3 kPa. This point can be seen in Fig. 10d, showing that practically the entire pressure drop generated in this case occurs in the final region of the channel. Thus, we can observe that the slug passage in the narrow part of the channel induces a much more significant pressure drop and that the slug length is the most important parameter in relation to determining the pressure drop.

Besides the pressure, other transport variables in the channel will be affected by the multiphase nature of the flow, which is particularly important to the velocity field. In Fig. 11 we can observe the velocity profile along the central line of the channel for some

selected time steps. This profile represents the total velocity magnitude, not a component of the velocity vectors. Moreover, in Fig. 11 the respective liquid water distribution can be seen with some of the normalized vector fields shown in detail. Fig. 11a shows a time step before the formation of large slugs, with a predominance of homogeneous droplets. In the initial region the velocity profile exhibits an oscillatory behavior produced by the continuous constraint and expansion in the free space caused by the presence of droplets. In the second half of the channel the droplets have a height greater than half of the entire channel height and therefore the central line passes through the droplets. As we can observe, the velocity magnitude in the droplets and in the gaps between droplets reduces to a very small value, which is indicative of the stagnation generated by the presence of the droplets. This stagnation is harmful to the fuel cell performance because it hinders oxygen transport to the GDL surface.

In the insets of Fig. 11a two different patterns for the flow inside the droplets are shown. Near the channel inlet, two anti-symmetric eddies appears, as also observed in Fig. 5b. As the channel becomes narrower and the air velocity increases, the shear forces become more significant and the flow pattern inside the droplets changes, inducing the formation of a single anti-clockwise eddy. Thus, the

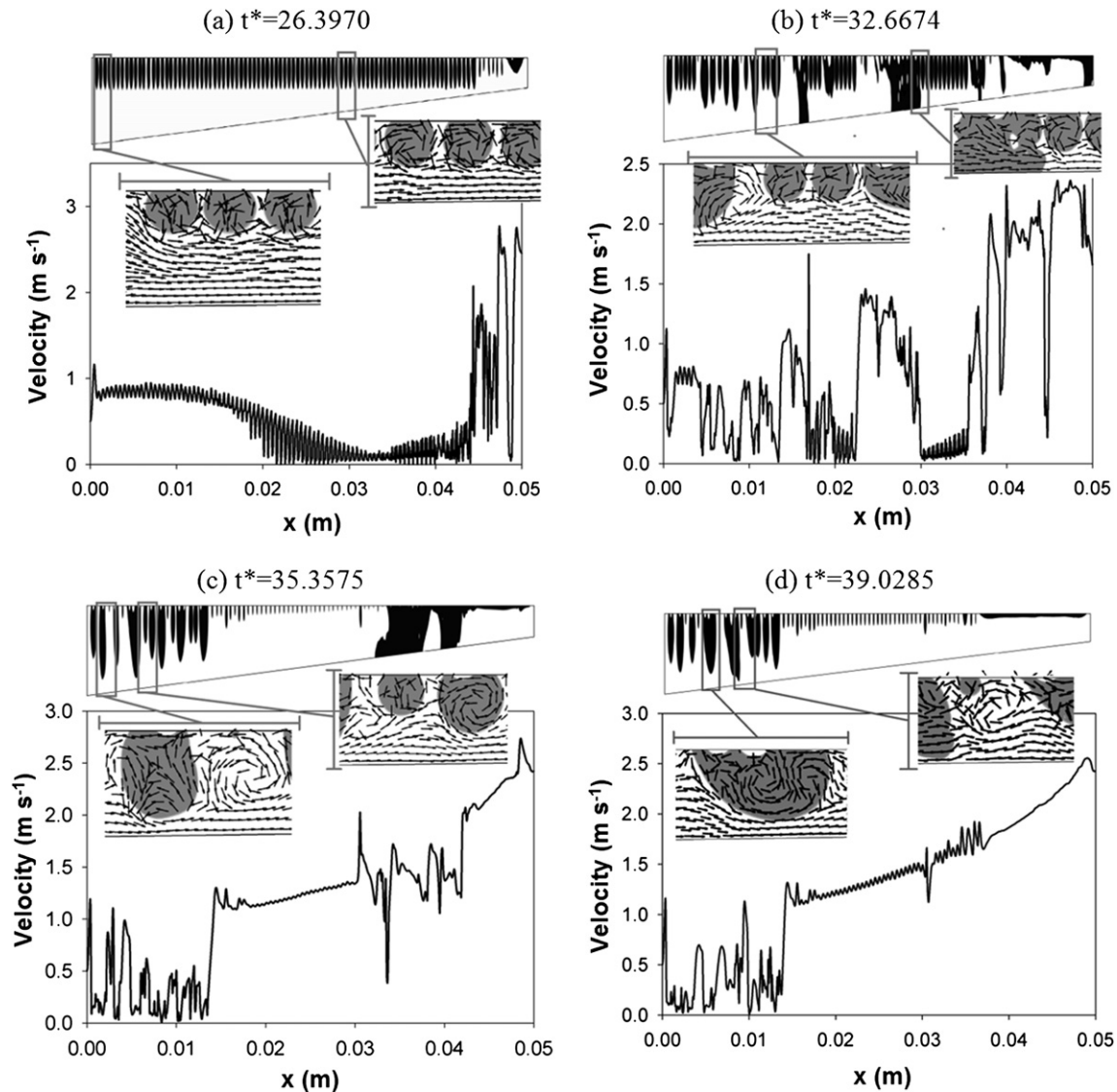


Fig. 11. Liquid water presence within the channel (upper part) and velocity profile along central line of the channel for selected time-steps.

flow configuration inside the droplets is dependent upon the air velocity and the droplet size. This can be clearly seen in Fig. 11c, where the picture in the inset shows two adjacent droplets with different flow patterns. Fig. 11b shows the velocity profile for a time step with the presence of a large slug. No recirculation is noted within the slug, indicating that the entire mass of liquid water moves with an approximately constant velocity toward the channel outlet. This can also be noted for the slug region in the velocity profile shown in Fig. 11c. The presence of a film covering the GDL surface makes the velocity profiles become non-oscillatory, as can be seen in Fig. 11d. Thus, the velocity profile can be considered indicative of the flow regime allowing, in most cases, the determination of the droplet length, film formation and slug presence.

4. Conclusions

In this study the volume of fluid method was employed to investigate the gas and liquid water transport inside a tapered flow channel. A two-dimensional, dynamic and isothermal model was used to determine the velocity, pressure and phase distribution inside a tapered channel with an inclination of 0.75° and a total length of 5 cm. The boundary conditions were defined to represent

a real operational condition, with several liquid water inlets on the GDL surface. The results revealed the strong influence of the channel inclination, with different flow regimes appearing simultaneously in different regions. Considering the operational conditions, the surface tension is the predominant force and, as a consequence, the droplets initially show a practically homogeneous growth along the entire channel, assuming a spherical shape. When the droplets become large enough, coalescence and detachment can be observed, which occurs firstly near the channel outlet. Depending upon the conditions of air velocity and droplet size the mass of liquid water can assume the form of a slug or a film. Near the channel outlet, due to the higher gas velocity, the formation of a liquid film on the GDL surface can be observed, while in the central part and near the channel inlet the main form of liquid water transport is as slugs. As they move toward the channel outlet, the slugs capture the growing droplets, which contributes to the removal of the liquid water and a reduction in the water saturation. The tapered channel was found to favor the slug formation, thus assisting the water management. However, the presence of slugs accentuates considerably the pressure drop, especially when passing through the narrowest region, and therefore the parasitic losses associated with the gas compression increase, making

a careful study necessary to determine whether the gain in the fuel cell output is sufficient to compensate for these costs.

Acknowledgments

The authors are grateful to CNPq (process: 143152/2011-4) for financial support. Helpful suggestion by Professors F. Greco and G. Continillo are warmly acknowledged.

References

- [1] K. Tüber, M. Zobel, H. Schmidt, C. Hebling, J. Power Sources 122 (2003) 1–8.
- [2] F. Alcaide, G. Álvarez, J.B. Blázquez, P.L. Cabot, O. Miguel, Int. J. Hydrogen Energy 35 (2010) 5521–5527.
- [3] D. Hissel, M.C. Péra, J.M. Kauffmann, J. Power Sources 128 (2004) 239–246.
- [4] U.S. Selamogullari, T.R. Willemain, D.A. Torrey, J. Power Sources 171 (2007) 802–810.
- [5] M.M. Mench, Fuel Cell Engines, John Wiley and Sons, 2008.
- [6] K. Jiao, X. Li, Prog. Energy Combust. Sci. 37 (2011) 221–291.
- [7] K.T. Cho, M.M. Mench, J. Power Sources 195 (2010) 6748–6757.
- [8] G.G. Park, Y.J. Sohn, T.H. Yang, Y.G. Yoon, W.Y. Lee, C.S. Kim, J. Power Sources 131 (2004) 182–187.
- [9] S. Park, B.N. Popov, Fuel 88 (2009) 2068–2073.
- [10] T. Kim, S. Lee, H. Park, Int. J. Hydrogen Energy 35 (2010) 8631–8643.
- [11] J. Chen, H. Xu, H. Zhang, N. Yi, J. Power Sources 182 (2008) 531–539.
- [12] F. Urbani, O. Barbera, G. Giaccoppo, G. Squadrito, E. Passalacqua, Int. J. Hydrogen Energy 33 (2008) 3137–3141.
- [13] J.P. Owejan, J.J. Gagliardo, J.M. Sergi, S.G. Kandlikar, T.A. Trabold, Int. J. Hydrogen Energy 34 (2009) 3436–3444.
- [14] Z. Lu, S.G. Kandlikar, C. Rath, M. Grimm, W. Domigan, A.D. White, M. Hardbarger, J.P. Owejan, T.A. Trabold, Int. J. Hydrogen Energy 34 (2009) 3445–3456.
- [15] I.S. Hussiani, C.Y. Wang, J. Power Sources 187 (2009) 444–451.
- [16] T.C. Wu, N. Djilali, J. Power Sources 208 (2012) 248–256.
- [17] Q. Yan, H. Toghiani, H. Causey, J. Power Sources 161 (2006) 492–502.
- [18] J.J. Baschuk, X. Li, J. Power Sources 86 (1–2) (2000) 181–196.
- [19] Fluent 13.0 Documentation, Fluent Inc., 2010.
- [20] K. Jiao, B. Zhou, P. Quan, J. Power Sources 157 (2006) 226–243.
- [21] X. Wang, B. Zhou, J. Power Sources 196 (2011) 1776–1794.
- [22] A. Le, B. Zhou, J. Power Sources 193 (2009) 665–683.
- [23] P. Quan, B. Zhou, A. Sobiesiak, Z. Liu, J. Power Sources 152 (2005) 131–145.
- [24] A.D. Le, B. Zhou, H.R. Shiu, C. Lee, W.C. Chang, J. Power Sources 195 (2010) 7302–7315.
- [25] Z. Zhan, J. Xiao, M. Pan, R. Yuan, J. Power Sources 160 (2006) 1–9.
- [26] A.D. Le, B. Zhou, J. Power Sources 182 (2008) 197–222.
- [27] H. Kim, J.H. Nam, D. Shin, T.Y. Chung, Y.G. Kim, Curr. Appl. Phys. 10 (2010) S91–S96.
- [28] A.D. Le, B. Zhou, Electrochim. Acta 54 (2009) 2137–2154.
- [29] L. Chen, T.F. Cao, Z.H. Li, Y.L. He, W.Q. Tao, Int. J. Hydrogen Energy 37 (2012) 9155–9170.
- [30] X. Zhu, Q. Liao, P.C. Sui, N. Djilali, J. Power Sources 195 (2010) 801–812.
- [31] X. Zhu, P.C. Sui, N. Djilali, J. Power Sources 181 (2008) 101–115.
- [32] P. Quan, M.C. Lai, J. Power Sources 164 (2007) 222–237.
- [33] Y. Ding, H.T. Bia, D.P. Wilkinson, J. Power Sources 196 (2011) 6284–6292.
- [34] Y. Ding, H.T. Bi, D.P. Wilkinson, J. Power Sources 195 (2010) 7278–7288.

- [35] Y. Cai, T. Chen, T. Yang, J. Xiao, J. Power Sources 209 (2012) 90–104.
- [36] É. Fontana, E. Mancusi, A. Silva, V.C. Mariani, A.A.U. Souza, S.G.U. Souza, Int. J. Heat Mass. Transfer 54 (2011) 4462–4472.
- [37] S.W. Perng, H.W. Wu, Appl. Energy 88 (2011) 52–67.
- [38] H.C. Liu, W.M. Yan, C.Y. Soon, F. Chen, H.S. Chu, J. Power Sources 158 (2006) 78–87.
- [39] Z. Zhenzhong, C. Junxun, Z. Pingji, Chin. J. Chem. Eng. 17 (2) (2009) 286–297.
- [40] N. Akhtar, P.J.A.M. Kerkhof, Int. J. Hydrogen Energy 36 (2011) 3076–3086.
- [41] E.D. Wang, P.F. Shi, C.Y. Du, Electrochem. Commun. 10 (2008) 555–558.
- [42] C.H. Cheng, H.H. Lin, G.J. Lai, J. Power Sources 165 (2007) 803–813.
- [43] Z. Lu, C. Rath, G. Zhang, S.G. Kandlikar, Int. J. Hydrogen Energy 36 (2011) 9864–9875.
- [44] C.E. Colosqui, M.J. Cheah, I.G. Kevrekidis, J.B. Benziger, J. Power Sources 196 (2011) 10057–10068.
- [45] Z. Zhan, C. Wanga, W. Fu, M. Pan, Int. J. Hydrogen Energy 37 (2012) 1094–1105.
- [46] M. Grimm, E.J. See, S.G. Kandlikar, Int. J. Hydrogen Energy 37 (2012) 12489–12503.
- [47] N. Kapur, P.H. Gaskell, Phys. Rev. E 75 (2007) 056315.
- [48] C.H. Schillberg, S.G. Kandlikar, A Review of Models for Water Droplet Detachment from the Gas Diffusion Layer – Gas Flow Channel Interface in PEMFCs, in: Proceedings of the Fifth International Conference on Nano-channels, Microchannels and Minichannels, ICNMM2007–30029 (2007).

Nomenclature

Bo: bond number
Ca: capillary number
C_k: volume fraction of the *k*th fluid
d_p: width of the water inlets (m)
g: gravity vector (0, m s^{−2})
H: channel height (m)
L: channel length (m)
n: vector normal to the surface
n_w: unit vectors normal to the wall
p: pressure (atm)
R: radius orthogonal to the surface (m)
t: time (s)
T: operation temperature (K)
t_w: unit vectors normal to the wall
*t**: dimensionless time
u: velocity vector (m s^{−1})
u_i: liquid water inlet velocity (m s^{−1})
We: Weber number
x, y: Cartesian coordinates (m)

Greek alphabet
θ: channel bottom wall inclination
θ_w: static contact angle
κ: surface curvature (m^{−1})
μ: viscosity (kg m^{−1} s^{−1})
ρ: density (kg m^{−3})
σ: surface tension (N m^{−1})

Superscripts and subscripts

1: gas phase
 2: liquid phase